Article

Advanced Science, Engineering and Medicine
Vol. 8, 1–8, 2016
www.aspbs.com/asem

Copyright © 2016 American Scientific Publishers
All rights reserved
Printed in the United States of America

Gum Mediated Synthesis and Characterization of Indium Oxide (In_2O_3) Nanoparticles

Ch. Kanchana Latha[1], Y. Aparna[1,*], and Ramchander Merugu[2]

[1] *Department of Physics, JNTUH, CEH, Kukatpally, Hyderabad, Telangana, India*
[2] *Department of Biochemistry, Mahatma Gandhi University, Nalgonda, Telangana, India*

Biological synthesized nanoparticles are simple, cost effective and eco-friendly and have many applications in various sectors. Hence, in the present study, biosynthesis of nanoparticles from plants which are emerging as nano-factories has been investigated. Yellowish In_2O_3 nanoparticles have been biologically synthesized using *Indium(III) Acetylacetonate* as precursor via *Acacia nilotica* gum and was characterized by TG-DTA to determine the thermal decomposition and crystallization temperature was found to be at above 450 °C. Nanoparticles are formed after calcination of the precursor of In_2O_3 in air at 470 °C–650 °C for 2 hours. The obtained In_2O_3 nanoparticles were characterized by UV-Vis Spectroscopy, XRD, SEM, EDAX, TEM, and PL. The crystalline size of In_2O_3 nanoparticles was increased from 12 to 17 nm up on increasing the sintering temperature from 500 °C to 650 °C. The prepared In_2O_3 nanoparticles showed a strong PL emission in the UV region. The strong emissions of In_2O_3 are attributed to the radiative recombination of an electron occupying the oxygen vacancies with a photo excited hole. The present work proves that the *Acacia nilotica* gum extracted synthesis is a novel and useful method using cheap precursors for preparation of In_2O_3 nanoparticles.

Keywords: Gum Mediated Synthesis, Indium Oxide Nanoparticles, XRD, UV-Vis, TEM, PL, SEM, EDAX.

1. INTRODUCTION

Indium Oxide (In_2O_3) is a Transparent Conductor Oxide (TCO), which has a cubic bixbyite structure with a wide band-gap of 3.55–3.75 eV. It has high electron affinity, high transparency to visible light and high electrical conductance.[1,2] Indium Oxide (In_2O_3) structures are obtained in various forms such as nanobelts,[3–5] nanofibres,[6,7] nanowires[8–15] and nanoparticles.[16–18] They have been widely used in Sensors,[19,20] Solar cells,[21–23] Ultra violet photo detectors,[24,25] Photo electro chemical cells[26] and Photo catalysis.[27] There are different methods to synthesize In_2O_3 nanoparticles such as Sol–gel technique,[28–30] Pulse laser deposition,[16] Thermal decomposition,[18,28–31] Spray Pyrolysis,[32] Mechanical/Chemical processing,[33] Hybrid Induction and Laser Heating (HILH) method,[34] Non-aqueous synthesis,[35] Hydro thermal synthesis[36] and Green synthesis method.[37–40]

Nanoparticles obtained from plant extracts are more stable than other Green synthesis method (Bacteria, Actinomycetes, Yeasts, Fungi and Algae). Among these plant extracts Gum mediated synthesis is a novel synthesis which gives high yield compared to other plant extracts. Because in Gum mediated synthesis there are no physical and chemical methods and it eliminates the use and generation of hazardous substances.[41] The choice of solvents, reducing agent employed and the dispersing agents increase interest in identifying eco-friendly materials which are multi functional and the procedure involved is simple and less time consuming. Acacia nilotica gum exudes from the trunk and is used as a soothing agent in inflammatory conditions and has been used for the stabilization of In_2O_3 nanoparticles.

2. EXPERIMENTAL DETAILS

2.1. Synthesis of In_2O_3 Nanoparticles

For the preparation of Indium Oxide nanoparticles, the chemical materials used were Indium(III) Acetylacetonate

*Author to whom correspondence should be addressed.

(99.99 + % purity, Sigma Aldrich) and Acacia nilotica (Acacia Gum) bought from Unani (*davaa saas*) Shop at Hyderabad. As shown in Figure 1, the Indium(III) Acetylacetonate (3 gm) and Acacia nilotica (0.3 gm) were mixed and crushed into fine powder using mortar and pistle. The precursor was characterized by TG-DTA (Fig. 2) to determine the calcination temperature and is found to be above 450 °C. Then the precursor was calcined in box furnace at 500 °C, 550 °C and 650 °C for 2 hours in air. The yellowish nanopowders of In_2O_3 were obtained.

2.2. Physical Characterization

The dried precursors and calcined samples of yellowish In_2O_3 were characterized for crystal phase identification by powder X-ray Diffraction (XRD) using a Philips X-ray Diffractometer with CuK_α radiation ($\lambda = 0.15406$ nm). The particle size and morphology of the calcined powders were characterized by TEM (Transmission Electron Microscopy), HRTEM (High Resolution Transmission Electron Microscopy) and SEM (Scanning Electron Microscopy) and chemical composition by EDAX (Energy Dispersive Analysis of X-rays). The optical absorption spectra were measured in the range of 200–800 nm using a UV-Vis scanning spectrometer. Photoluminescence (PL) measurement was carried out on a Luminescence Spectrometer using a Xenon lamp as the excitation source at room temperature. The samples were dispersed in ethylene glycol and dichloromethane respectively. The excitation wave length in PL measurement was 383 nm.

3. RESULTS AND DISCUSSION

3.1. TG-DTA Analysis

The Thermo Gravimetric Differential Thermal Analysis (TG-DTA) curves of as-prepared In_2O_3 precursor are shown in Figure 2. The TG curve in Figure 2 shows a major weight loss step from 200 °C upto about 450 °C and no further weight loss was observed above 700 °C. The weight loss is related to the combustion of organic matrix. On the DTA curve (Fig. 2), a main exothermic effect was observed between 450 °C and 500 °C with a maximum at about 470 °C indicating that the thermal events can be associated with the burnout of organic species involved in the precursor powders (organic mass remained from Acacia gum) of the residual carbon or due to direct crystallization of nanocrystalline In_2O_3 from the amorphous component.

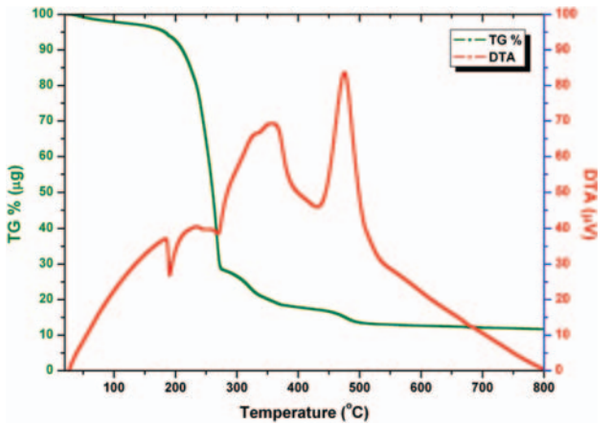

Figure 2. TG-DTA curves of thermal decomposition of In_2O_3 precursor at a heating rate of 10 °C/min in static air.

The formation of nanocrystalline In_2O_3 as decomposition product was confirmed by XRD and TEM results shown in Figures 3 and 4.

3.2. XRD Analysis

The XRD patterns of In_2O_3 samples are shown in Figure 3. All of the detectable peaks (Fig. 3) can be indexed as the In_2O_3 cubic structure in the standard data

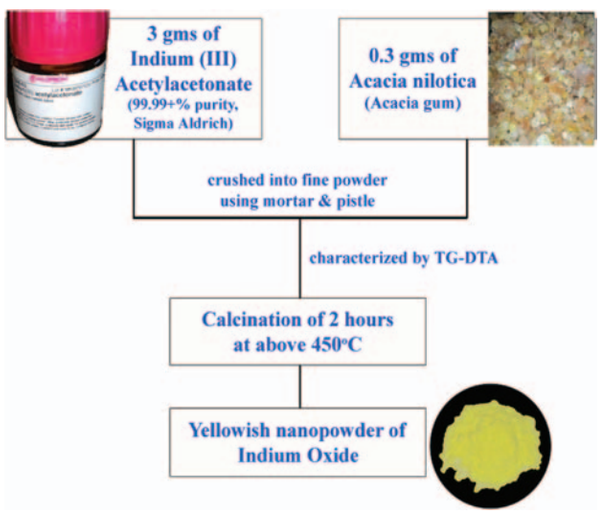

Figure 1. Flow chart of preparation of In_2O_3 nanoparticles.

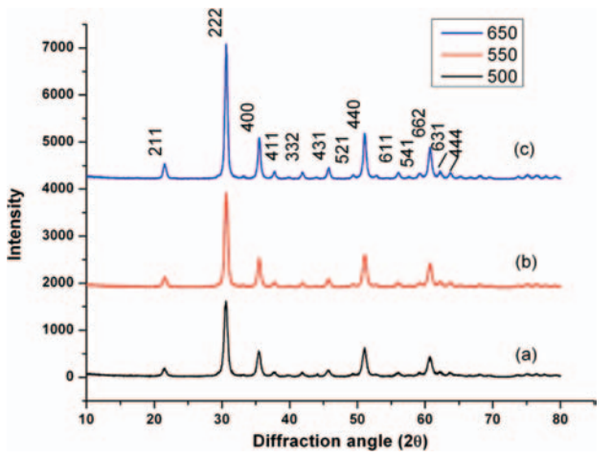

Figure 3. XRD patterns of nanocrystalline In_2O_3 samples calcined in air for 2 hours at (a) 500 °C (b) 550 °C and (c) 650 °C.

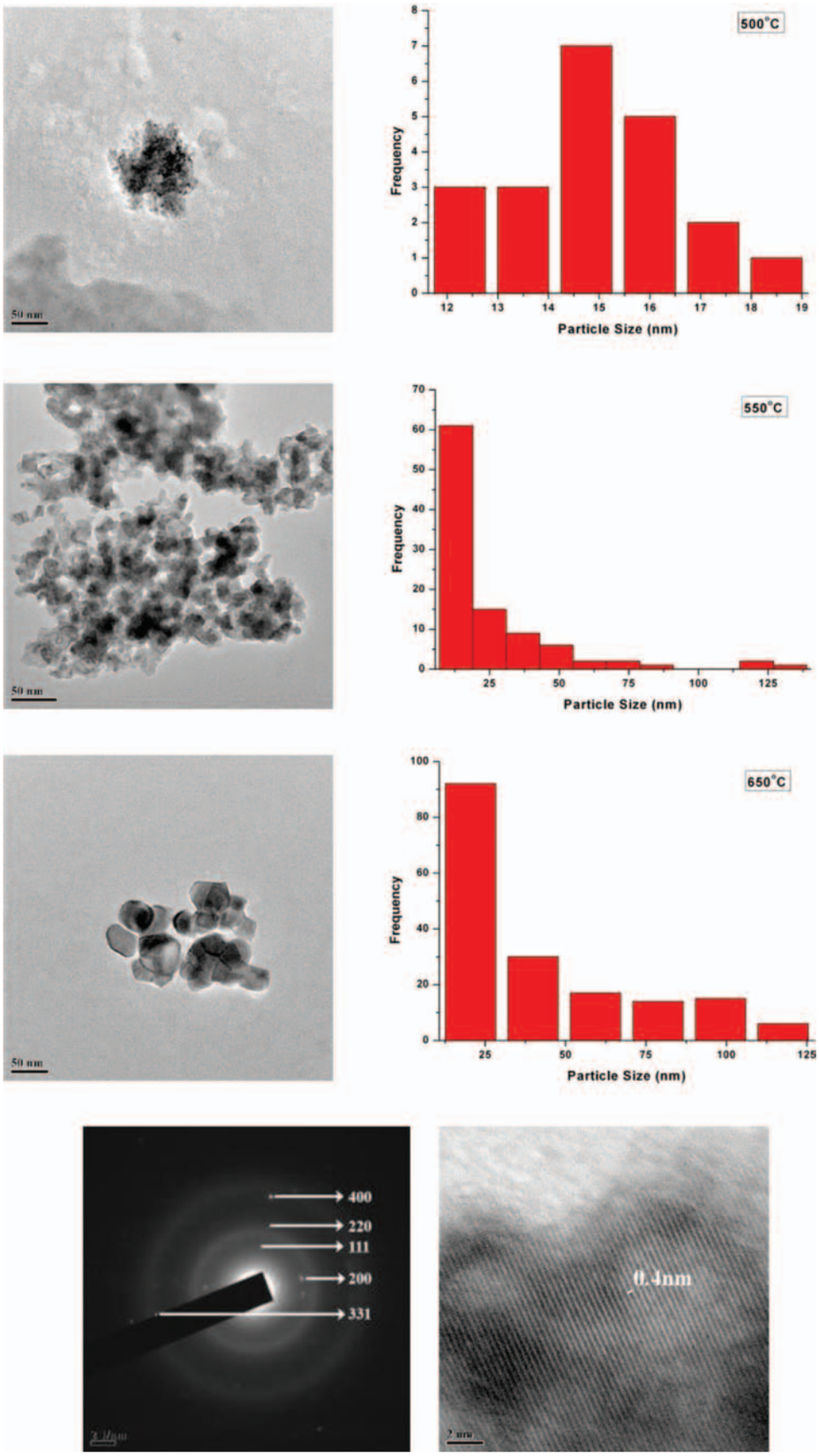

Figure 4. Continued.

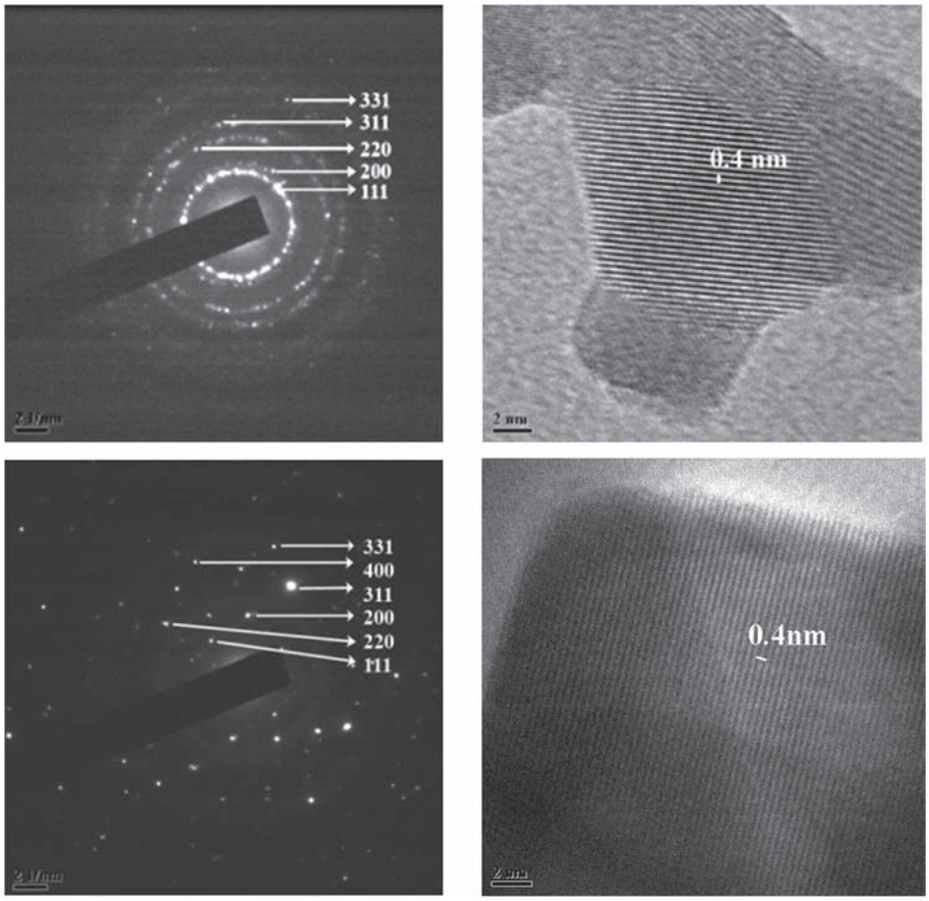

Figure 4. TEM images with particle size distribution and corresponding SAED patterns and HRTEM of the nanocrystalline In_2O_3 samples calcined in air for 2 hours at (a) 500 °C, (b) 550 °C, (c) 600 °C.

(JCPDS: 06-0416). The cubic lattice parameter 'a' calculated from the XRD spectra for (222) plane are (10.126 Å, 10.1107 Å and 10.1095 Å), and their d_{hkl} (2.92333, 2.91880 and 2.91846) and FWHM values (0.6359, 0.5380 and 0.4586) are for In_2O_3 samples calcined at 500 °C, 550 °C and 650 °C respectively. Evidence of the bixbyite symmetry was confirmed by the non-symmetric line shape around ($2\theta = 30.558°$ and 60.6°) regions in the XRD pattern are close to those of lattice constants $a = 10.117$ Å in the standard data (JCPDS: 06-0416). The crystalline sizes of the powders are estimated from X-ray line broadening using Scherrer Equation[42] (i.e., $D = 0.89\lambda/(\beta \cos\theta)$, where λ (=0.15406 nm) is the wave length of the X-ray radiation, k is a constant taken as 0.89, θ is the diffraction angle β is the Full Width at Half Maximum (FWHM) and were obtained to be (12 nm, 15 nm and 17.8 nm)

Table I. Average particle sizes from XRD line broadening cubic lattice parameter 'a' calculated from HRTEM and the band gap (E_g) of the nanocrystalline In_2O_3 samples calcined in air at different temperatures for 2 hours.

In_2O_3 calcined at temperature (in °C)	Average particle size (nm) from		Cubic lattice parameter from HRTEM 'a' (nm)	Estimated band gap (eV) from UV-data	Bru's formula particle size (nm)
	XRD	TEM			
500	12	12–19	0.6928	3.824	10.373
550	15	27	0.6928	3.83	9.686
650	17	27	0.6928	3.89	9.623

Table II. Interplanar spacing (d_{hkl}) of In_2O_3 samples calculated from TEM selected area electron diffraction patterns in Figure 4 compared with the reference values in the standard data (JCPDS :06-0416).

	Calcined interplanar spacing (d_{hkl}) In_2O_3 sample (Å)				
	In_2O_3 sample calcined at			Standard data (JCPDS: 06-0416)	
Ring	500°C	550 °C	600 °C	d_{hkl} (Å)	hkl
R_1	3.236	3.067	3.389	3.1234	111
R_2	2.525	2.59	2.638	2.7056	200
R_3	1.984	1.96	1.805	1.9134	220
R_4	1.245	1.257	1.2722	1.2414	331
R_5	1.36	–	1.3850	1.353	400
R_6	–	1.639	1.605	1.6318	311

for In_2O_3 samples calcined at 500 °C, 550 °C and 650 °C respectively. The particle sizes and lattice parameters are of In_2O_3 samples are also summarized in Table I. This fact did convey that higher the temperature of calcination applied to In_2O_3 nanoparticles, better is its crystallinity.[43]

3.3. TEM Analysis

The morphology and structure of the In_2O_3 samples were investigated by TEM. It is clear from the TEM bright field images (Fig. 4) that the morphology and size of In_2O_3 materials is affected by the calcination temperature. The TEM nanoparticle size of In_2O_3 (Fig. 4) show that the In_2O_3 sample calcined at 500 °C, 550 °C and 650 °C having sizes of ~12–19 nm, ~27 nm and ~27 nm respectively and the HRTEM interplanar spacing bright-field images are 0.4 nm ($a = 0.6928$ nm in Table I) at 500 °C, 550 °C and 650 °C. These lattices can be attributed to the plane of (111) of In_2O_3. The corresponding Selected Area Electron Diffraction (SAED) patterns (Fig. 4) of all the In_2O_3 samples showed with a pattern of round marks called *Spotty Ring Patterns* without any additional diffraction spots and rings of second phases, revealing their crystalline cubic structure. Increase in calcination temperature results in stronger spotty pattern and the In_2O_3 samples calcined at 550 °C and 650 °C shows strong spotty patterns than at 500 °C, indicating large particle size of highly crystalline cubic structure. Measured interplanar spacings (d_{hkl}) from selected area electron diffraction patterns in Figure 4 are in good agreement with the values in the standard data (JCPDS: 06-0416) as summarized in Table II.

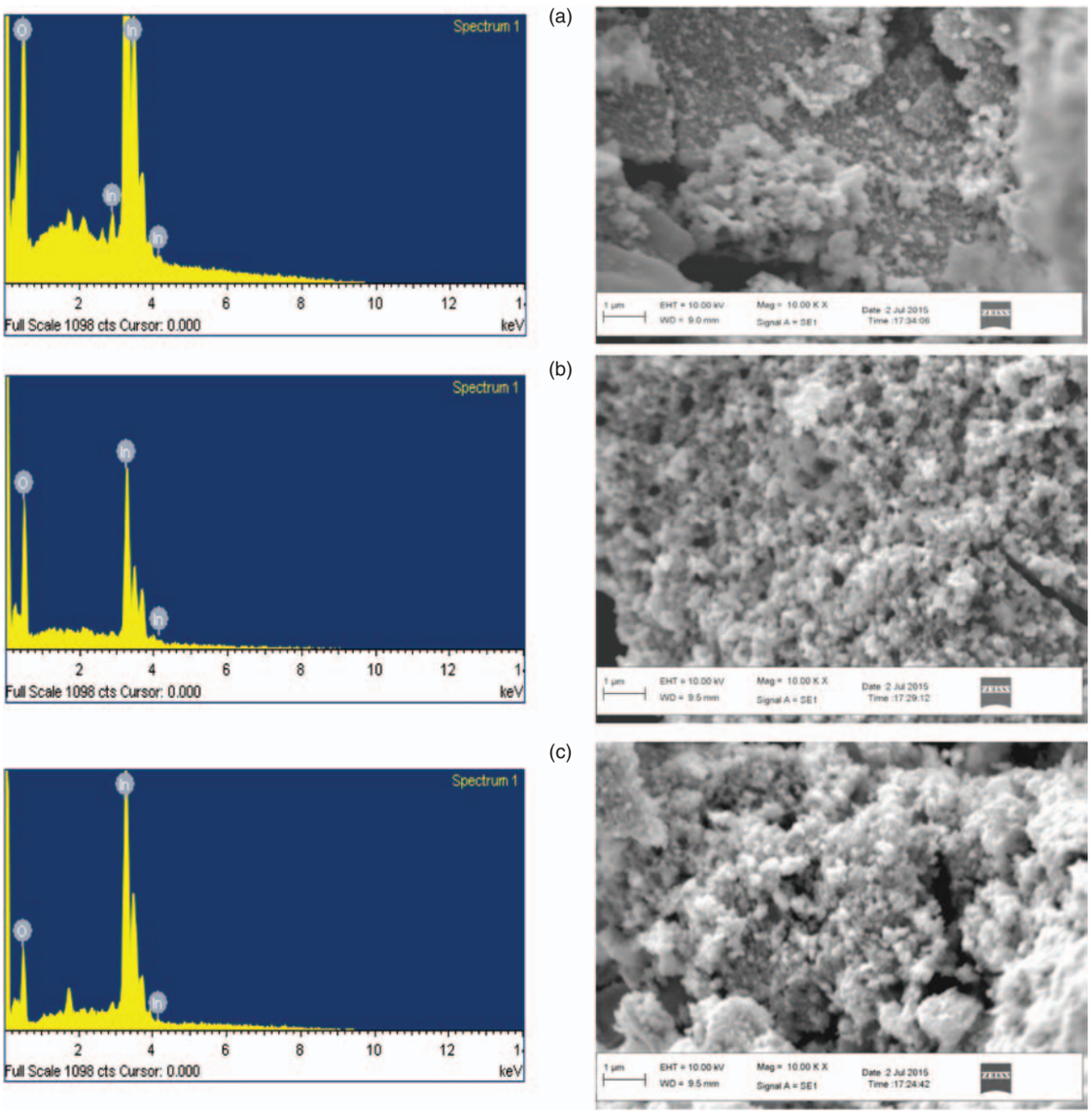

Figure 5. EDAX and SEM images of the nanocrystalline In_2O_3 at (a) 500 °C (b) 550 °C and (c) 650 °C.

3.4. EDAX and SEM Analysis

The SEM images in Figure 5 showed that the In_2O_3 nanoparticles are formed as cubic crystals. However, the particle size as well as agglomeration increased and the smaller grains coalesced to form larger sized particles[43] with increase in the calcination temperature. These images reflect that the In_2O_3 nanoparticles are nearly spherical in morphology along with the poly dispersed distribution of particle size. But the degree of poly dispersity is observed to be small. In addition, the agglomeration of In_2O_3 nanoparticles in all the samples increases but appears to be less. This is due to the capping of In_2O_3 nanoparticles by Acacia gum. The usage of Acacia gum is effectively preventing the In_2O_3 nanoparticles from agglomeration and therefore controlling the size of In_2O_3 nanoparticles, however, with the increase in the calcination temperature.

The EDAX data at 500 °C sintering temperature suggested the stoichiometry of In_2O_3 nanoparticles with the elemental composition of Oxygen and Indium and their atomic percentages are given in Table III. The atomic ratio of O/In calculated as 1.90 at 500 °C indicated the stoichiometric composition of In_2O_3 which is in good agreement with the theoretical value of 1.50.[44] But at 550 °C, the nanopowder exhibits some impurities such as Carbon which are recorded along with the strong signals of In and O atoms. The weight and atomic percentages of each element extracted from the Quantitative (EDAX) Analysis are listed in Table III.

3.5. UV-Vis Absorbance

Now let us consider the optical properties of the In_2O_3 samples. The UV-Visible absorption spectra of all the In_2O_3 samples (Fig. 6) exhibit a strong absorption below (470 nm) (2.76 eV) with a well defined absorbance peak at around 272 nm (4.59 eV).

The direct band gap energy (E_g) of the samples is determined by fitting the absorption data to the direct transition equation: $\alpha h\nu = E_d(h\nu - E_g)^{1/2}$ where α is the optical absorption coefficient, $h\nu$ is the photon energy, E_g is the direct band gap, and E_d is a constant.[45] Plotting $(\alpha h\nu)^2$ as a function of photon energy, and extrapolating the linear portion of the curve to the absorption equal to zero as shown in the insets of Figure 4 gives the values of the direct band gap (E_g) to be 3.824 eV, 3.83 eV and 3.89 eV for the In_2O_3 samples calcined at 500 °C, 550 °C and 600 °C respectively. This value is

Table III. EDAX data of In_2O_3 samples calcined in air for 2 hours at 500 °C, 550 °C and 650 °C.

	Indium		Oxygen	
Temperature	Weight %	Atomic %	Weight %	Atomic %
500 °C	78.08	33.39	21.42	65.74
550 °C	64.49	21.83	29.95	72.77
650 °C	82.76	40.22	14.61	50.96

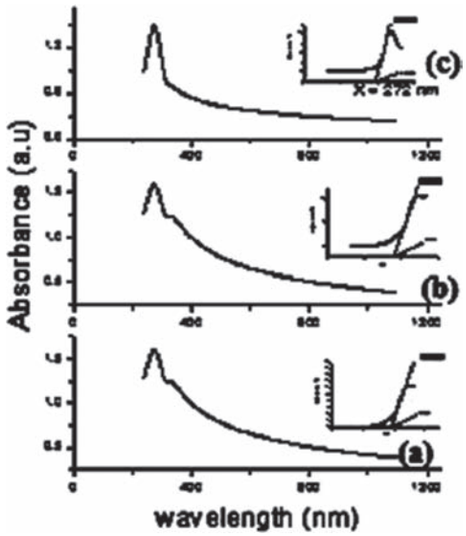

Figure 6. Room temperature optical absorbance spectre of nanocrystalline In_2O_3 samples calcined in air for 2 hours at (a) 500 °C (b) 550 °C (c) 600 °C. The insets showplots of $(\alpha h\nu)^2$ as a function of photon energy.

higher than that of ~3.75 eV for the In_2O_3 reported in the literature.[46] It can be noted that the band gap values increases with increasing the calcination temperature. This may be due to increase in particle size, which results in band gap between the valence band and conduction band of In_2O_3 nanoparticles. When red shift is observed the particle size increased with increasing sintering temperature as observed in Table I (*Bru's formula*) using the band gap from UV-Vis spectrum.[29]

$$\text{Brus formula } E_{g_n} = \left[E_{g_b}^2 + \left\{\frac{2h^2E_{g_b}(\pi/R)^2}{m^*}\right\}\right]^{1/2} \quad (1)$$

where R—Radius of the nanoparticle; E_g and E_{gb} are the band gaps of the nanoand bulk systems respectively, and $m^* = 0.9\ m_o$ is the effective mass of electron

3.6. PL Spectrum

Figure 7 shows the room temperature PL spectra of the nanocrystalline In_2O_3 samples measured using a Xenon laser of 250 nm as an excitation source. The spectra of all the samples mainly consists of a strong UV emission broadband having emission maximum at ~{383 nm (4.6 eV)}. The spectra of all the samples also show a weak UV band at ~383 nm (4.6 eV). It is well known that the bulk In_2O_3 cannot emit light at room temperature.[47] However PL emissions of our nanocrystalline In_2O_3 samples are possibly due to the effect of the oxygen vacancies as reported in literature.[5, 7, 8, 17, 18, 48–52] In the present work, oxygen vacancies would be generated due to partial or incomplete oxidation of precursor during the calcinations. Moreover small In_2O_3 particles would favor the existence of oxygen vacancies as found in In_2O_3 nanowires with high aspect ratios and high surface to volume ratio.[5, 7, 44]

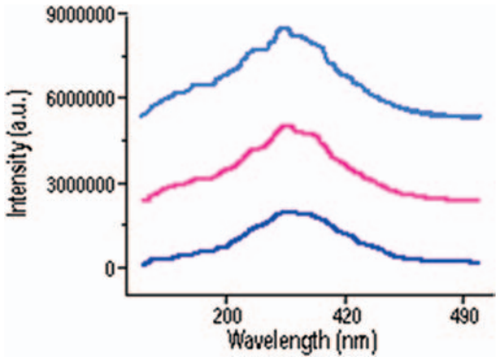

Figure 7. Room temperature Photoluminescence spectra of the synthesized nanocrystalline In_2O_3 samples calcined in air for (a) 600 °C, (b) 550 °C and (c) 500 °C.

The oxygen vacancies would generally act as deep defect donors and cause the formation of new energy levels in the band gap of In_2O_3 samples. Thus, the PL emission from In_2O_3 nanoparticles results from the radiative recombination of electron occupying oxygen vacancies with a photo excited hole, which is analogous to the photo luminescence mechanism of ZnO and SnO_2 semiconductors.[5, 49, 51] It is clearly seen from TEM results (Fig. 4) that as the calcinations temperature increases, the crystal size of In_2O_3 samples become larger. As a result, the number of sensitizing centers decreases owing to reduction in both the ratio surface area and concentration of oxygen vacancies which results in a decrease in PL intensity as observed in ZnO nanoparticles reported by Du et al.[43]

4. CONCLUSION

Phase pure, cubic In_2O_3 nanoparticles were prepared by biosynthesis method by sintering Indium Acetyl Acetonate and Acacia gum. Structural, morphological and optical properties of the synthesized nanoparticles were characterized. XRD and TEM analysis showed that there is an increase in crystallite size and percentage of crystallinity with increasing sintering temperature and it is observed from UV-Vis data that the band gap value, particle size of In_2O_3 nanoparticles increases with increasing temperature. The Photoluminescence spectra of In_2O_3 nanoparticles obtained with higher sintering temperatures showed no reduction in the emission intensity due to oxygen vacancies. The present work proves that the Acacia gum extract is a new useful method using cheap precursors for preparation of In_2O_3 nanoparticles. The current simple, cost effective and environmental friendly synthesis method using Acacia gum powder gives a potential avenue for further practical scale-up of the production process and application.

References and Notes

1. C. G. Granquist, *Appl. Phys. A: Solids Surf.* 57, 19 (**1993**).
2. K.G. Gopachandran, B. Joseph, J. T. Abraham, P. Koshy, and V. K. Vaidyan, *Vacunum* 48, 547 (**1997**).
3. J. S. Jeong, J. Y. Lee, C. J. Lee, S. J. An, and G.-C. Yi, *Chem. Phys. Lett.* 384, 246 (**2004**).
4. T. Gao and T. Wang, *J. Cryst. Growth.* 290, 660 (**2006**).
5. C. H. Liang, G. W. Meng, Y. Lei, F. Phillipp, and L. D. Zhang, *Adv. Mater.* 13, 1330 (**2001**).
6. Y. Zhang, J. Li, Q. Li, L. Zhu, X. Liu, X. Zhong, J. Meng, and X. Cao, *Scripta Mater.* 56, 409 (**2007**).
7. X. S. Peng, Y. W. Wang, J. Zhang, X. F. Wang, L. X. Zhao, G. W. Meng, and L. D. Zhang, *Appl. Phys. A* 74, 437 (**2002**).
8. X. C. Wu, J. M. Hong, Z. J. Han, and Y. R. Tao, *Chem. Phys. Lett.* 373, 28 (**2003**).
9. J. Lao, J. Huang, D. Wang, and Z. Ren, *Adv. Mater.* 16, 65 (**2004**).
10. K. Kam, F. L. Deepak, A. K. Cheetham, and C. N. R. Rao, *Chem. Phys. Lett.* 297, 329 (**2004**).
11. Y. Zhang, H. Ago, J. Liu, M. Yumura, K. Uchida, S. Ohshima, S. Iijima, J. Zhu, X. Zhang, and J. Cryst, *Growth* 264, 363 (**2004**).
12. S. Q. Li, Y. X. Liang, and T. H. Wang, *Appl. Phys. Lett.* 88, 053107 (**2006**).
13. S. Kar, S. Chakrabarti, and S. Chaudhuri, *Nanotechnology* 17, 3058 (**2006**).
14. G. Cheng, E. Stren, S. Guthrie, M. A. Reed, R. Klin, Y. Hao, G. Meng, and L. Zhang, *Appl. Phys. A* 85, 233 (**2006**).
15. A. Murali, A. Barve, V. L. Leppert, and S. H. Risbud, *NanoLett.* 1, 287 (**2001**).
16. W. S. Seo, H. H. Jo, K. Lee, and J. T. Park, *Adv. Mater.* 15, 795 (**2003**).
17. Z. Zhan, W. Song, and D. Jiang, *J. Colloid Interf. Sci.* 271, 366 (**2004**).
18. A. Gurlo, M. Ivanovskaya, N. Barsan, M. Shweizer-Berberich, U. Weimar, W. Gopel, and A. Dieguez, *Sens. Actuat. B* 44, 327 (**1997**).
19. S. Elouali, L. G. Bloor, R. Binions, I. P. Parkin, C. J. Carmalt, and J. A. Darr, *Langmuir* 28, 1879 (**2012**).
20. Leed, J. Ondrake, and T. Cui, *Sensors* 11, 9300 (**2011**).
21. A. L. Dawar and J. C. Joshi, *J. Mater. Sci.* 19, 1 (**1984**).
22. H. L. Hartnagel, A. L. Dawar, A. K. Jain, and C. J. Jagadish, Semi-Conducting Transp Thin Films, IOP, Bristol (**1995**).
23. B. G. Lewis and D. C. Paine, *MRS Bull.* 25, 22 (**2000**).
24. D. Shao, L. Qin, and S. Sawyer, *IEE Photon J.* 4, 715 (**2012**).
25. D. Zhang, C. Li, Hans, X. Liu, T. Tang, W. Jin, and C. Zhou, *Appl. Phys. A* 77, 163 (**2003**).
26. Ganj, Lux, Wuj, Xies, Zhait, M. Yu, Z. Zhang, Y. Mao, S. C. L. Wang, Y. Shen, Y. Tong, *Sci. Rep.* 3, 1021 (**2013**).
27. K. R. Reyes-Gil, E. A. Reyes-Garcia, and D. Raftery, *J. Phys. Chem. C* 111, 14579 (**2007**).
28. M. Ivanovskaya, A. Gurlo, and P. Bogdanov, *Sens. Actuat. B* 77, 264 (**2001**).
29. M. Epifani and P. Siciliano, *J. Am. Chem. Soc.* 126, 4078 (**2004**).
30. X. J. Wu and J. Vac. *Sci. Technol.* 15, 1889 (**1997**).
31. J. J. Prince, S. Ramamurthy, and B. Subramanian, *J. Cryst. Growth* 240, 142 (**2002**).
32. H. Yang, A. Tang, X. Zhang, W. Yang, and G. Qiu, *Scripta Mater.* 50, 413 (**2004**).
33. B. L. Zhu, C. S. Xie, D. W. Zeng, A. H. Wang, W. L. Song, and X. Z. Zhao, *J. Mater. Sci. Lett.* 0022 (**2005**).
34. M. Niederberger, G. Garnweitner, J. Buha, J. Polleux, J. Ba, and N. Pinna, *J. Sol–Gel Sci. Tech.* 40, 259 (**2006**).
35. J. Xu, X. Wang, and J. Shen, *Sens. Actuat. B* 115, 642 (**2006**).
36. B. D. Cullity and S. R. Stock, Elements of X-ray Diffraction, 3rd edn., Printice Hall, New Jersey (**2001**).
37. S. Iravani, *Green Chem.* 13, 2638 (**2011**).
38. Ch. Sreelakshmi, N. Goel, K. K. R. Datta, A. Anthony, Ummanni Ramesh, and B. V. Subba Reddy, *Nanosci. Nanotechnol. Lett.* 5, 1258 (**2013**).
39. S. Madhusudana Reddy, K. K. R. Datta, Ch. Sreelakshmi, M. Eswaramoorthy, and B. V. Subba Reddy, *Nanosci. Nanotechnol. Lett.* 4, 420 (**2012**).

40. Ch. Sreelakshmi, K. K. R. Datta, J. S. Yadav, and B. V. Subba Reddy, *J. Nanosci. Nanotechnol.* 8, 6995 **(2011)**.
41. P. T. Anastas and J. C. Warner, Green Chemistry, Theory and Practice, Oxford University Press Inc. New York **(1998)**.
42. E. Ziegler, A. Heinrich, H. Oppermann, and G. Stover, *Phys. Status Solidi A* 66, 635 **(1981)**.
43. Y. Du, M. S. Zhang, J. Hong, Y. Sheen, Q. Chen, and Z. Yin, *Appl. Physics A* 76, 171 **(2003)**.
44. J. I. Jeong, J. H. Moon, J. H. Hong, J. S. Kang, Y. Fukuda, Y. P. Lee, and J. Vac, *Sci. Technol. A* 14, 293 **(1996)**.
45. C. G. Granqvist, *Appl. Phys. A* 57, 19 **(1993)**.
46. Y. Ohhata, F. Shinoki, and S. Yoshida, *Thin Solid Films* 59, 255 **(1979)**.
47. M. S. Lee, W. C. Choi, E. K. Kim, C. K. Kim, and S. K. Min, *Thin Solid Films* 279, 1 **(1996)**.
48. H. J. Zhou, W. P. Cai, and L. D. Zhang, *Appl. Phys. Lett.* 75, 495 **(1999)**.
49. J. Zhang, X. Qing, F. Jiang, and Z. Dai, *Chem. Phys. Lett.* 371, 311 **(2003)**.
50. Q. Tang, W. Zhou, W. Zhang, S. Ou, K. Jiang, W. Yu, and Y. Qian, *Cryst. Growth Des.* 5, 147 **(2005)**.
51. M. A. F. Mendoza, R. C. Perez, G. T. Delgado, J. M. Marin, and O. Z. Angel, *Thin Solid Films* 517, 681 **(2008)**.
52. J. S. Cruz, G. T. Delgado, R. C. Perez, S. H. Sandoval, O. J. Sandoval, C. I. Z. Romero, J. M. Marin, and O. Z. Angel, *Thin Solid Films* 83, 493 **(2005)**.

Received: 27 October 2015. Accepted: 28 January 2016.